# Chemical Trend of Transition-Metal Doping in $WSe_2$

Dan Han,[1,2,3] Wenmei Ming,[3] Haixuan Xu,[4] Shiyou Chen,[1,*] Deyan Sun,[2] and Mao-Hua Du[3,†]

[1] *Key Laboratory of Polar Materials and Devices (Ministry of Education), East China Normal University, Shanghai 200241, China*

[2] *Department of Physics, East China Normal University, Shanghai 200241, China*

[3] *Materials Science and Technology Division, Oak Ridge National Laboratory, Oak Ridge, Tennessee 37831, USA*

[4] *Department of Materials Science and Engineering, The University of Tennessee, Knoxville, Tennessee 37996, USA*

(Received 10 June 2019; revised manuscript received 27 August 2019; published 19 September 2019)

Transition-metal dichalcogenides (TMDs) are promising nanoscale materials with a wide range of applications. Chemical doping is a powerful tool for tailoring the physical and chemical properties of TMDs for targeted functionalities. As one of the most important TMDs, $WSe_2$ has great potential for applications in field effect transistor and complementary metal oxide semiconductor technologies for its bipolar dopability. However, precise control over the type and density of free carriers remains challenging. First-principles calculations are performed to study intrinsic defects and transition-metal (TM) dopants in $WSe_2$. Our results show that TM doping can effectively control the Fermi level in $WSe_2$ with no significant compensation by intrinsic defects. Nb and Ta are effective *p*-type dopants capable of generating a high free hole density in $WSe_2$. While *n*-type doping is possible by Re (under the Se-rich condition) and Cu (under the W-rich condition), the doping efficiency is reduced due to the lower attainable dopant concentration and higher ionization energies. The chemical trend in the attainable concentration of various substitutional TM dopants in $WSe_2$ is largely determined by the competition between the dopant incorporation in $WSe_2$ and the formation of the secondary phase $TMSe_2$. Such a competition is strongly affected by the different crystal environments of the TM ion in $TMSe_2$ and $WSe_2$, which determine the crystal field splitting and electron filling of TM *d* levels and consequently the formation energy of the TM dopant.

DOI: 10.1103/PhysRevApplied.12.034038

## I. INTRODUCTION

Layered transition-metal dichalcogenides (TMDs) have been extensively studied for their unique properties and a wide range of applications, including field-effect transistors (FETs) [1,2], batteries [3,4], supercapacitors [5,6], photovoltaics [7,8], and catalysis [9,10]. In particular, the atomic-scale thickness without surface dangling bonds and sizable band gaps render TMDs promising nanoelectronic materials [11–16]. The ability to dope two-dimensional (2D) TMDs, both *n*- and *p*-types, with high carrier density and mobility as well as air and thermal stability is essential to the development of FET and complementary meta-oxide-semiconductor (CMOS) technologies [17–19]. However, this has not been realized in 2D TMDs, thus inhibiting further technology development.

Among many TMDs, $WSe_2$ appears promising for FET and CMOS applications due to both *p*- and *n*-type dopability. $WSe_2$ has an indirect band gap of 1.4 eV [20,21]. Both *p*-type and *n*-type conductivities have been reported for undoped bulk $WSe_2$ with carrier densities on the order of $10^{15}$ or $10^{16}$ $cm^{-3}$ [21–25]. Chemical doping has been shown to improve *p*- and *n*-type conductivities [26,27]. Nb and Ta doping enhanced *p*-type conductivity in bulk and monolayer $WSe_2$ [26–29] while Re, In, and Cu doping led to *n*-type conductivity [22,27,30,31]. Although these results demonstrated bipolar doping of $WSe_2$, the efficiencies of *n*- and *p*-type doping are asymmetric. Degenerate doping of $WSe_2$ crystals by Nb with a hole density $>10^{19}$ $cm^{-3}$ has been reported, whereas the highest electron density in *n*-type $WSe_2$ by substitutional doping is only on the order of $10^{17}$ $cm^{-3}$ [27]. Surface charge transfer doping by chemisorption and physisorption of metal atoms and organic molecules is another approach to modulate the carrier type and carrier density in $WSe_2$ [1,32–40]. Degenerate *n*-type doping by K in few-layer $WSe_2$ has been reported [34]. However, the application of the surface charge transfer doping may be limited due to the relatively poor air and thermal stability as well as the incompatibility with conventional semiconductor technologies [41].

Despite the critical importance of chemical doping in the functionalization of 2D TMDs, the underlying mechanisms that determine the doping efficiency are still

*chensy@ee.ecnu.edu.cn
†mhdu@ornl.gov

 

poorly understood. Theoretical studies of TM dopants in $WSe_2$ have been limited to neutral dopants [42,43]; the critical information on dopant formation energies, dopant-induced charge transition levels, and Fermi-level pinning by dopants is still lacking. In this paper, we investigate intrinsic point defects and a series of dopants (Nb, Ta, Re, Ru, Os, Cu, Ag, and In) in bulk $WSe_2$ using first-principles calculations. The results show that the formation energy of a TM dopant in $WSe_2$ can be substantially lower than those of intrinsic defects. Thus, the TM doping can determine the Fermi level. We also find a large variation in the minimal formation energy of TM dopants in $WSe_2$. The different ligand environments of TM dopants in $WSe_2$ and $TMSe_2$ secondary phases play an important role in the competition of dopant stability in $WSe_2$ and in secondary phases, which determines the minimal dopant formation energy and the attainable dopant concentration.

## II. COMPUTATIONAL METHOD

All calculations are based on density functional theory (DFT) [44,45] implemented in the VASP code [46]. The interaction between ions and electrons is described by the projector augmented wave method [47] and the kinetic energy cut off is set to 350 eV. The total energy is obtained by the Perdew-Burke-Eznerhof (PBE) exchange correlation functional [48] while the band gap is corrected by using the hybrid HSE06 functional [49]. The van der Waals interaction is included using the DFT-D2 method [50] to account for the important interlayer coupling in $WSe_2$. To calculate the formation energy of a defect, a $6 \times 6 \times 1$ hexagonal supercell ($a = b = 19.957$ Å and $c = 12.768$ Å) containing 216 atoms and a $\Gamma$ point centered $1 \times 1 \times 2$ $k$-point mesh are used. The atomic positions are relaxed until the forces are less than 0.01 eV/Å.

The calculated band gap of bulk $WSe_2$ at the PBE level is 0.90 eV, which is underestimated due to the well-known band gap error in PBE calculations. The band gap is corrected by using the hybrid HSE06 functional [49] with the fraction of the Hartree-Fock exchange adjusted to 20%. The HSE06-corrected band gap is 1.39 eV, which is in good agreement with the experimentally measured band gap of 1.40 eV [20,21].

The formation energy of a defect or a dopant is given by

$$\Delta H = (E_D - E_h) - \sum_i n_i(\mu_i + \mu_i^{\mathrm{ref}}) + q(\varepsilon_{\mathrm{VBM}} + \varepsilon_F), \tag{1}$$

where $E_D$ and $E_h$ are the total energies of the defect-containing and the host (i.e., defect-free) supercells. The formation of a defect in a material involves an exchange of atoms with their respective chemical reservoirs. The second term in Eq. (1) represents the change in energy due to such an exchange of atoms, where $n_i$ is the difference in the number of atoms for the $i$th atomic species between the defect-containing and defect-free supercells. $\mu_i$ is the relative chemical potential for the $i$th atomic species, referenced to the chemical potential of its elemental phase $\mu_i^{\mathrm{ref}}$. The third term in Eq. (1) represents the change in energy due to the exchange of electrons with its reservoir. $\varepsilon_{\mathrm{VBM}}$ is the energy of the valence band maximum (VBM) and $\varepsilon_F$ is the Fermi energy relative to the VBM. The VBM and the conduction band minimum (CBM) from the PBE calculation are corrected using the band gap from the HSE06 calculation as described above. The shallow defect levels, which mainly have the character of bulk electronic states, are shifted with their respective band edges, while the deep levels, which are highly localized, are not corrected since they are not expected to move significantly following the band-gap correction. Previous calculations of defect levels using this approach compare very well with full hybrid functional calculations of both the total energy and the band gap [51–53]. Corrections to the defect formation energy due to potential alignment (between the host and a charged defect supercell), band filling, and image charge corrections are applied wherever appropriate following the approach described in Ref. [54]. The calculated dielectric matrix shows the in-plane and out-of-plane dielectric constants of 16.11 and 7.93, respectively. The average dielectric constant, which is taken as the trace of the dielectric matrix (13.38), is used when calculating the image charge correction.

The chemical potentials in Eq. (1) are subject to a series of thermodynamic constraints under the equilibrium growth condition. To maintain the stability of $WSe_2$ during growth, the chemical potentials of W and Se should satisfy

$$\mu_{\mathrm{W}} + 2\mu_{\mathrm{Se}} = \Delta H_f(\mathrm{WSe_2}), \tag{2}$$

where $\Delta H_f(\mathrm{WSe_2})$ is the enthalpy of formation for $WSe_2$.

To avoid the formation of the elemental phases of W, Se and the dopant $X$ ($X =$ Nb, Ta, Re, Ru, Os, Cu, Ag, and In), the following constraints on chemical potentials are applied

$$\mu_{\mathrm{W}} < 0, \mu_{\mathrm{Se}} < 0, \mu_X < 0. \tag{3}$$

Since the dopant $X$ may react with Se to form secondary phases $X_n\mathrm{Se}_m$, we further apply the following constraints to suppress the secondary phase formation

$$n\mu_X + m\mu_{\mathrm{Se}} \leq \Delta H_f(X_n\mathrm{Se}_m), \tag{4}$$

where $\Delta H_f(X_n\mathrm{Se}_m)$ is the enthalpy of formation for the secondary phase $X_n\mathrm{Se}_m$. The dopant formation energy is calculated by taking the maximum allowed dopant chemical potential. We consider all possible secondary phases shown in the Materials Project [54] (a Materials genome database) for each dopant. Taking the Nb dopant as an

example, we considered Nb selenide compounds of $NbSe_2$, $NbSe_3$, $NbSe_4$, $Nb_2Se_3$, $Nb_3Se_4$, $Nb_2Se_9$, and $Nb_5Se_4$. Among all the potential secondary phases, those constraining the dopant chemical potential are found to be $NbSe_2$ ($P6_3/mmc$), $TaSe_2$ ($P6_3/mmc$), $ReSe_2$ ($P\bar{1}$), $RuSe_2$ ($Pa$-3), $OsSe_2$ ($Pa$-3), CuSe ($Cmcm$), $Ag_2Se$ ($P2_12_12_1$), and $In_2Se_3$ ($P6_1$).

The dopant concentration is calculated by

$$N = N_{\text{site}} e^{-\Delta H/k_B T}, \tag{5}$$

where $N_{\text{site}}$ is the number of available atomic sites for doping, $\Delta H$ is the dopant formation energy calculated by Eq. (1), $k_B$ is the Boltzmann constant, and $T$ is temperature.

## III. RESULTS AND DISCUSSION

The crystal structure of $WSe_2$ is shown in Fig. 1(a). There is only one inequivalent W site, and thus one substitutional site for metal doping. For interstitial defects and dopants, we consider the atop and hollow sites between two adjacent layers as well as the split interstitial, in which two atoms share one atomic site [see Fig. 1(b)].

Figure 2 shows the formation energies of intrinsic defects in $WSe_2$ under both W-rich and Se-rich conditions; the Se vacancy ($V_{\text{Se}}$) is an important acceptor defect under both conditions. This is consistent with previous DFT results in bulk and monolayer $MoS_2$, in which the S vacancy is the dominant electrically active defect [55,56]. The relatively low formation energy of $V_{\text{Se}}^0$ is due to the strong hybridization of the W-5$d$ orbitals adjacent to $V_{\text{Se}}$. The $d$-$d$ hybridization at $V_{\text{Se}}$ forms $a_1$ and $e$ levels [55]. At the neutral charge state, the $a_1$ level is fully occupied, creating an energy incentive for the three adjacent W cations to move closer to increase hybridization, thereby lowering the $a_1$ level [57]. The three W-W distances are reduced by 8% on average. As a result, the $a_1$ level of $V_{\text{Se}}^0$ is below the VBM and the empty $e$ level is inside the band gap

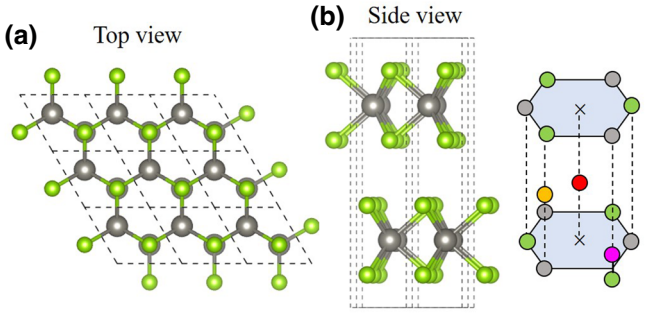


FIG. 1. (a) The crystal structure of $WSe_2$. Gray and green balls represent W and Se ions, respectively. (b) Schematic representations of three different interstitial sites: atop, hollow, and split interstitial sites. Red and orange balls indicate the locations of the hollow and atop sites, respectively. The purple ball represents the split interstitial, which shares the W site with a native W atom.

close to the CBM, rendering $V_{\text{Se}}$ a deep acceptor [with the (0/–) acceptor level calculated to be 1.19 eV above VBM (Fig. 2)] rather than an electron donor as would normally be expected for an anion vacancy. Since the (0/–) level of $V_{\text{Se}}$ is close to the CBM, $V_{\text{Se}}^0$ is stable in $p$-type and semi-insulating $WSe_2$, acting as an electron trap.

As can be seen in Fig. 2, the dominant intrinsic defects in $WSe_2$ are acceptors. At the W-rich limit [Fig. 2(a)], the density of $V_{\text{Se}}^0$, [$V_{\text{Se}}^0$], is calculated to be $2.87 \times 10^{12}$ cm$^{-3}$ using Eq. (5) at $T = 1000$ °C (growth temperature of $WSe_2$) [26,27]. The density of ionized $V_{\text{Se}}$, [$V_{\text{Se}}^-$], and the hole density (that balances [$V_{\text{Se}}^-$] for charge neutrality) should be even lower. At the Se-rich limit [Fig. 2(b)], the formation energy of $V_{\text{Se}}$ is higher than that at the W-rich limit [Fig. 2(a)]; thus, the hole density is not expected to exceed $10^{12}$ cm$^{-3}$. The experimentally measured hole or electron density on the order of $10^{15}$ or $10^{16}$ cm$^{-3}$ in undoped bulk $WSe_2$ [21–25] is likely due to charged impurities.

The above calculations show that intrinsic defects are not a significant source of free carrier generation in $WSe_2$. Next, we explore extrinsic dopants, including Nb, Ta, Re, Ru, Os, Cu, Ag, and In, in $WSe_2$ and develop an understanding of doping efficiency. Nb, Ta, and Re are the nearest neighbors to W in the periodic table, and thus are obvious choices for substitutional doping on the W site. These TM dopants as well as Cu and In have been investigated experimentally [22,26–31]. We perform calculations on all these dopants and a few of their neighbors in the periodic table (Ru, Os, Ag) to develop trends in their chemical stability.

The minimal formation energies of TM dopants under both the W-rich and Se-rich conditions are shown in Fig. 3. The maximum chemical potential of the TM dopant as determined by Eqs. (3) and (4) (the TM-rich limit) is used. The calculated enthalpies of formation for $WSe_2$ and various TM-dopant-related secondary phases are shown in Table S1 (Supplemental Material [58]); these values determine whether the TM chemical potential, $\mu_{\text{TM}}$, is limited by the elemental [Eq. (3)] or the binary [Eq. (4)] secondary phase.

Note that the formation energies of some TM dopants in Fig. 3 (i.e., $Nb_W$, $Ta_W$, $Ru_W$, $Os_W$) do not change from the W-rich limit [Fig. 3(a)] to the Se-rich limit [Fig. 3(b)]. This is because, for these dopants, $\mu_{\text{TM}}$is limited by the secondary phase $TMSe_2$ at both the W-rich and the Se-rich limits. Combining $\mu_{\text{TM}} + 2\mu_{\text{Se}} = \Delta H_f(TMSe_2)$ (the TM-rich limit) and $\mu_{\text{W}} + 2\mu_{\text{Se}} = H_f(WSe_2)$ [Eq. (2)], the chemical potential term in the formation energy [Eq. (1)] of a substitutional TM dopant, $TM_W$, can be shown to be $-\mu_{\text{TM}} + \mu_{\text{W}} = \Delta H_f(WSe_2) - \Delta H_f(TMSe_2)$, which is independent of the W or Se chemical potential. Such behavior results from the fact that the secondary phase $TMSe_2$ has the same cation-anion composition ratio as that of $WSe_2$. For other substitutional TM dopants, the TM chemical potential is limited

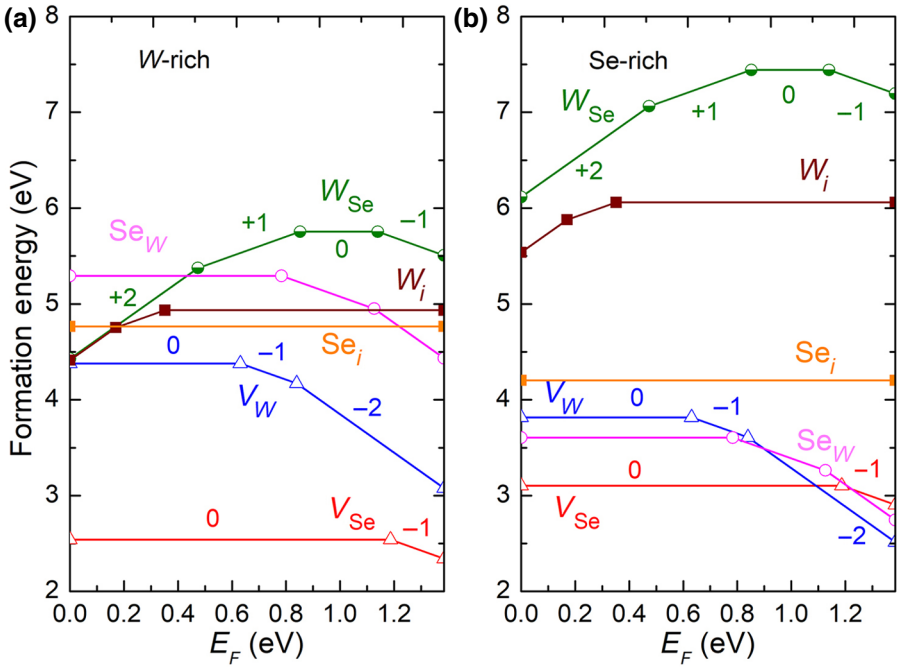


FIG. 2. Formation energies of intrinsic defects in $WSe_2$ as a function of the Fermi level under (a) W-rich and (b) Se-rich conditions. The energy of the VBM is set to zero. The slope of a formation energy line indicates the charge state of a defect, which is shown for selected defects. The Fermi level at which the slope changes, indicates a charge transition level.

by $\mu_{TM} + 2\mu_{Se} \leq \Delta H_f(TMSe_2)$ at the Se-rich limit, but by $\mu_{TM} \leq 0$ at the W-rich limit: Therefore, their formation energies change from the Se-rich limit to the W-rich limit. For interstitial TM dopants (Cu, Ag), the maximum TM chemical potential is limited by the secondary phase (i.e., CuSe, $Ag_2Se$), which contains Se; thus, the formation energy calculated at the TM-rich limit depends on the Se chemical potential.

As can be seen in Fig. 3, $Nb_W$ and $Ta_W$ have low formation energies and shallow acceptor levels. Thus, $Nb_W$ and $Ta_W$ should be efficient $p$-type dopants, consistent with the experimental findings of high doping level and high hole density $5.2 \times 10^{19}\,cm^{-3}$ [26–29]. $Re_W$ is the most stable electron donor. $Re_W^0$ has a higher formation energy than $Nb_W^0$ and $Ta_W^0$; the calculated (+/0) level of $Re_W$ ($E_c - 0.20$ eV) is deeper than the (0/−) levels of

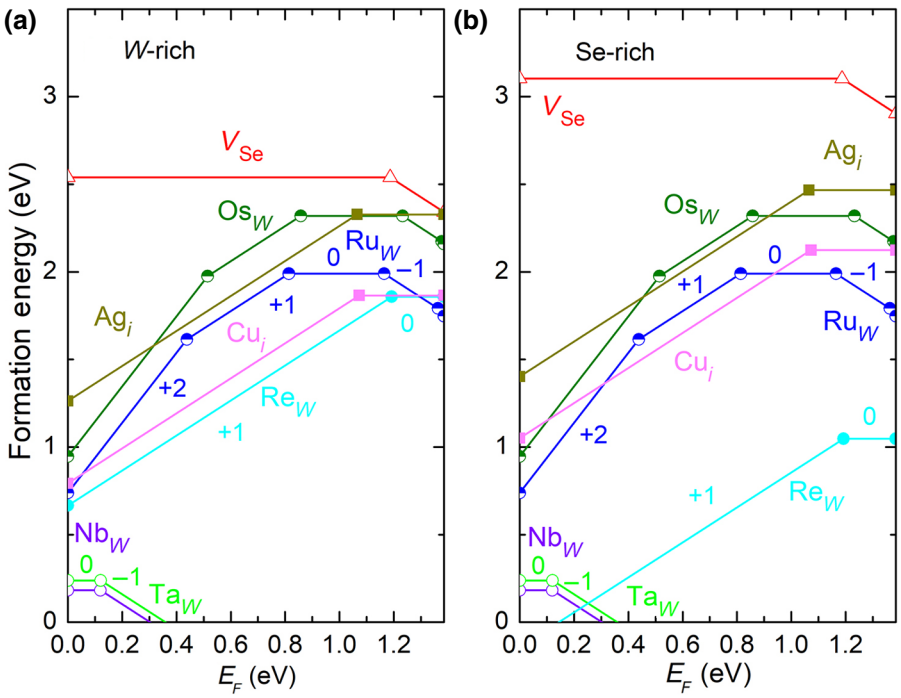


FIG. 3. Minimal formation energies of TM dopants (Nb, Ta, Re, Ru, Os, Cu, Ag) in $WSe_2$ as a function of the Fermi level under (a) W-rich and (b) Se-rich conditions. The maximum chemical potential of the TM dopant corresponding to the TM-rich limit, as determined by Eqs. (3) and (4), is used. The formation energy of $V_{Se}$ is shown for comparison. The energy of the VBM is set to zero. The slope of a formation energy line indicates the charge state of a defect or dopant, which is shown for selected dopants. The Fermi level at which the slope changes indicates a charge transition level.

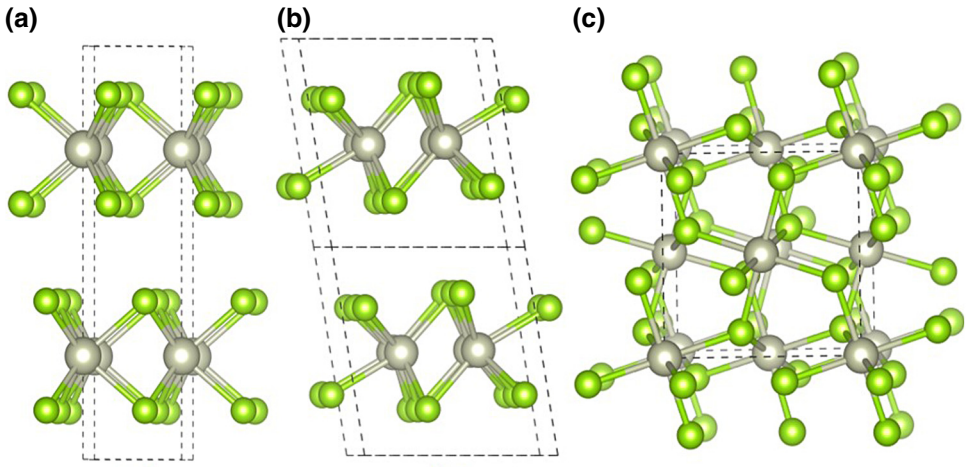


FIG. 4. Crystal structures of secondary phases of (a) $NbSe_2$ and $TaSe_2$ ($P_{63}/mmc$), (b) $ReSe_2$ ($P\bar{1}$), and (c) $RuSe_2$ and $OsSe_2$ ($Pa$-3). A TM ion has a trigonal prismatic coordination in (a) and a distorted octahedral coordination in (b),(c). Green and gray balls represent Se and TM ions, respectively.

$Nb_W$ and $Ta_W$ (both at $E_v + 0.12$ eV), consistent with the experimental finding of relatively low free electron density in Re-doped $WSe_2$ ($6.3 \times 10^{17}$ cm$^{-3}$) [27]. The relatively deep (+/0) level of $Re_W$ is due to a Re-induced bound state below the CBM, which is produced primarily by the *d-d* coupling between the Re dopant and the adjacent W ions. Notably, the formation energies of $Nb_W$, $Ta_W$, and $Re_W$ are all lower than those of intrinsic defects in $WSe_2$ under both W-rich and Se-rich conditions. Therefore, there are no compensating defects that limit the doping level and the carrier density in *p*-doped $WSe_2$:Nb and $WSe_2$:Ta and in *n*-doped $WSe_2$:Re. The Fermi level should lie between the VBM and the (0/–) level of $Nb_W(Ta_W)$ in Na(Ta)-doped $WSe_2$ and between the CBM and the (+/0) level of $Re_W$ in Re-doped $WSe_2$. The maximum densities of $Nb_W^0$, $Ta_W^0$, and $Re_W^0$ (under Se-rich and TM-rich limits) calculated using Eq. (5) at $T = 1000$ °C (growth temperature of $WSe_2$) [26,27] are $3.17 \times 10^{21}$, $1.83 \times 10^{21}$, and $1.14 \times 10^{18}$ cm$^{-3}$, respectively. (The density of W in $WSe_2$ is $1.65 \times 10^{22}$ cm$^{-3}$.) The densities of the ionized dopants ($Nb_W^-$, $Ta_W^-$, and $Re_W^+$) and free carriers should be lower than those of $Nb_W^0$, $Ta_W^0$, and $Re_W^0$, respectively, because the Fermi level is between the band edge and the ionization level as described above. These results are consistent with the experimental trend: A hole density of $5.2 \times 10^{19}$ cm$^{-3}$ in $WSe_2$:Nb and electron density of $6.3 \times 10^{17}$ cm$^{-3}$ in $WSe_2$:Re [27].

The trend of minimal formation energies of $Nb_W^0$, $Ta_W^0$, and $Re_W^0$ in Fig. 3 can be understood by the competition between the dopant incorporation in $WSe_2$ and the formation of secondary phases. Equation (1) shows that for a given dopant, a higher dopant chemical potential leads to a lower dopant formation energy. The maximum dopant chemical potential is limited by the formation of secondary phases [Eqs. (3) and (4)]. A very high TM-dopant chemical potential in the growth of $WSe_2$:TM may lead to the formation of $TMSe_2$ or even TM metal secondary phases rather than TM-doped $WSe_2$. It would be difficult to dope $WSe_2$ with a TM atom if the TM atom is much more stable in the secondary phase $TMSe_2$ than in $WSe_2$. The maximum allowed TM chemical potential (TM-rich limit) corresponds to the borderline between forming single-phase $WSe_2$:TM and segregated phases of $WSe_2$ and $TMSe_2$. Below, we discuss the trend of minimal formation energies of substitutional TM dopants at the TM-rich and Se-rich limits. We focus on the TM-rich and Se-rich limits because these conditions promote the substitution of W by TM dopants.

Our calculations find that at the Se-rich limit, the maximum chemical potential of a TM dopant (Nb, Ta, or Re) is limited by the formation of the secondary phase $TMSe_2$. It can be shown that at the Se-rich and TM-rich limits, the formation energy [Eq. (1)] of a TM dopant is given by

$$\Delta H(\mathrm{TM_W}) = (E_D - \mu_{\mathrm{TM,bulk}}) - \Delta H(\mathrm{TMSe_2}) + C. \quad (6)$$

Here, $E_D$ is the total energy of the supercell that contains the TM dopant, $\mu_{\mathrm{TM,bulk}}$ is the chemical of potential of TM in bulk TM, and $\Delta H(\mathrm{TMSe_2})$ is the enthalpy of formation of $TMSe_2$. The last term $C$ in Eq. (6) is unrelated to the dopant: $C = -E_h + \Delta H(\mathrm{WSe_2}) + \mu_{\mathrm{W,bulk}} + q(\varepsilon_{\mathrm{VBM}} + \varepsilon_F)$, where $\mu_{\mathrm{W,bulk}}$ is the chemical potential of W in bulk W metal. The binding strengths between the TM dopant and its ligands in $WSe_2$ and in the secondary phase $TMSe_2$ are reflected in $(E_D - \mu_{\mathrm{TM,bulk}})$ and $\Delta H(\mathrm{TMSe_2})$, respectively, in Eq. (6). Therefore, the formation energy of the substitutional dopant in Eq. (6) is largely determined by the competition of the TM-Se coupling in $WSe_2$ and $TMSe_2$, which, in turn, is strongly affected by the different crystal field splitting of the TM *d* levels in different crystal environments. It should be emphasized that the existence of a stable secondary phase for a TM dopant does not necessarily mean that the TM doping would be difficult. For example, the calculated enthalpy of formation in Table S1 (Supplemental Material [58]) shows that $NbSe_2$ and $TaSe_2$ are chemically more stable than $ReSe_2$ (Supplemental Material [58]); however, the doping of Nb and Ta in $WSe_2$ is energetically more favorable

than the doping of Re based on the calculated dopant formation energies in Fig. 3. (This result also agrees with the experimental observation [27].) Therefore, what determines the formation energy of a $TM_W$ is the competition between the TM-Se bonding in $WSe_2$:TM and that in $TMSe_2$. A TM atom in $TMSe_2$ and a substitutional TM dopant in $WSe_2$ both form six TM-Se bonds. However, the six nearest Se neighbors to the TM atom in $WSe_2$ could have a different symmetry from those in $TMSe_2$, which strongly affects the formation energy of $TM_W$ as shown below.

$NbSe_2$ and $TaSe_2$ share the same crystal structure with $WSe_2$ (space group $P_{63}/mmc$). [See Fig. 4(a).] The TM ions in $NbSe_2$, $TaSe_2$, and $WSe_2$ all have the trigonal prismatic coordination and the $d$ levels undergo the same crystal field splitting as shown for $NbSe_2$ as an example in Fig. 5. $Nb^{4+}$ and $Ta^{4+}$ are both $d^1$ ions. Taking $Nb^{4+}$ as an example, the single $d$ electron in $Nb^{4+}$ in $WSe_2$ and in $NbSe_2$ occupies the same low-lying $d_{z^2}$ level. Thus, the incorporation of $Nb^{4+}$ in $WSe_2$ competes favorably with $Nb^{4+}$ in $NbSe_2$. On the other hand, $ReSe_2$ has a $P\bar{1}$ [59] crystal structure [Fig. 4(b)] and $Re^{4+}$ (a $d^3$ ion) has a distorted octahedral environment, in which the three $d$ electrons of $Re^{4+}$ occupy the low-lying nonbonding $d_{xy}$, $d_{xz}$, and $d_{yz}$ orbitals ($t_{2g}$) in the majority spin channel (see Fig. 5), opening up a sizable band gap (1.29 eV [60]) between the $t_{2g}$ and $e_g$ levels. When $Re^{4+}$ substitutes a $W^{4+}$ ion in $WSe_2$, one of the three $d$ electrons is forced into the higher-lying $d_{x^2-y^2,xy}$ orbital. Thus, the change of the crystal environment of $Re^{4+}$ from $ReSe_2$ to $WSe_2$ incurs a relatively high energy cost [a relatively high value of $(E_D - \mu_{\mathrm{TM,bulk}}) - \Delta H(\mathrm{TMSe_2})$ in Eq. (6)], resulting in a higher formation energy of $Re^0_W$ in $WSe_2$.

We further study Ru and Os dopants, which have one more $d$ electron than Re. The results show that the substitutional $Ru_W$ and $Os_W$ are amphoteric dopants in $WSe_2$, acting as donors when the Fermi level is low and as acceptors when the Fermi level is high. Doping $WSe_2$ with Ru or Os is expected to result in Fermi-level pinning deep inside the band gap with very low carrier density. Thus, Ru and Os are not good $n$- or $p$-type dopants in $WSe_2$. $RuSe_2$ and $OsSe_2$ have the pyrite crystal structure (space group $Pa$-3 [61,62]) as shown in Fig. 4(c), in which Ru and Os have a nominal oxidation state of 2+ (due to the formation of Se-Se dimers in the pyrite structure) and a distorted octahedral coordination. The six $d$ electrons in $Ru^{2+}$ and $Os^{2+}$ fill the low-lying $t_{2g}$ level [63]. On the other hand, $Ru^{2+}$ and $Os^{2+}$ in $WSe_2$ ($Ru^{2-}_W$ and $Os^{2-}_W$) fill the high-lying $d_{x^2-y^2,xy}$ levels and are not even thermodynamically stable. [The (–/2-) levels of $Ru_W$ and $Os_W$ are above the CBM.] This explains the high formation energies of $Ru_W$ and $Os_W$ as shown in Fig. 3.

We have also studied TM dopants (Nb, Ta, Re, Ru, Os) at interstitial sites. These interstitial TM dopants are found to have significantly higher formation energies in $WSe_2$ than the substitutional dopants, thus they are not shown in Fig. 3. The only TM dopants that we find to have relatively low formation energies for interstitials are Cu and Ag, which are stable at the hollow site as shown in Fig. 1(c). $Cu_W$ and $Ag_W$ have significantly higher formation energies than $Cu_i$ and $Ag_i$ and are shown in Figure S1 [Supplemental Material [58]]. Importantly, under the W-rich condition, the formation energy of $Cu_i$ is comparable to that of $Re_W$ as shown in Fig. 3. These results suggest that the $n$-type doping by Re and Cu should be performed under the Se-rich and W-rich conditions, respectively. There is indeed a report that showed effective Cu doping, which turns slightly $p$-type $WSe_2$ to slightly $n$-type [31]. However, the calculated ionization energy of $Cu_i$ is significant (0.32 eV below the CBM), which makes it difficult to obtain high free electron density in $WSe_2$:Cu. The high ionization energy of $Cu_i$ is the result of significant $s$-$d$ coupling between Cu and the adjacent W ions, which produces a bound state below the CBM. Our calculations show that $Ag_i$ has a significantly higher formation energy than $Cu_i$, which is likely due to the larger ionic radius of $Ag^+$ (1.15 Å) than $Cu^+$ (0.77 Å). We also study In dopant in $WSe_2$ motivated by the experimental result that In doping turns $p$-type $WSe_2$ to $n$-type [30]. However, our results show that In is not an effective dopant in $WSe_2$ because of the high formation energies for both substitutional and interstitial In and the compensation between $In_i$ (donor)

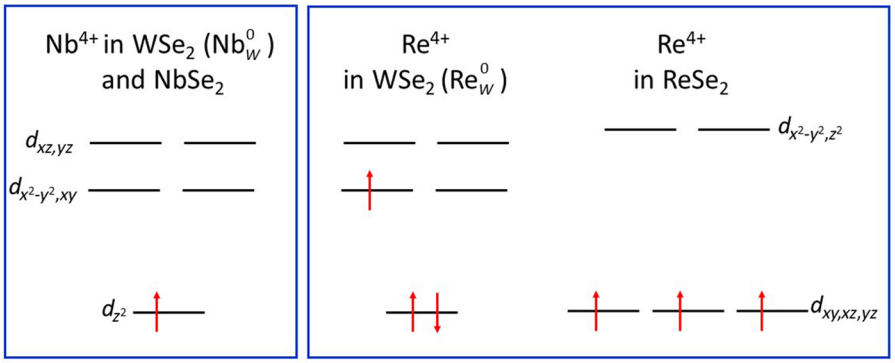


FIG. 5. Schematic of crystal field splitting and electron filling for $Nb^{4+}$ and $Re^{4+}$ in $WSe_2$ and their respective secondary phases $NbSe_2$ and $ReSe_2$.

and $In_W$ (acceptor) (Figure S1) (Supplemental Material [58]).

## IV. CONCLUSION

Intrinsic defects and TM dopants (Nb, Ta, Re, Ru, Os, Cu, Ag) in bulk $WSe_2$ are investigated using first-principles calculations. All intrinsic defects have relatively high formation energies and consequently low concentrations. $V_{Se}$ is the dominant intrinsic defect and $V_{Se}^0$ acts as a deep electron trap in $p$-type and semi-insulating $WSe_2$. Thus, intrinsic defects are not expected to introduce a significant number of free carriers in undoped $WSe_2$. All the TM dopants studied in this work have lower formation energies than those of intrinsic defects. $Nb_W$ and $Ta_W$ have the lowest formation energies and shallow acceptor levels, which can lead to a high level of $p$-type doping. In comparison, the most important $n$-type dopants, $Re_W$ and $Cu_i$, have relatively higher formation energies and deeper ionization energies, which can lead to $n$-type doping, but with lower free electron density. Our results show that the $n$-type doping is most effective by Re doping under the Se-rich condition and by Cu doping under the W-rich condition. The large variation in the minimal formation energy of various substitutional TM dopants is related to the secondary phases $TMSe_2$ because the maximal TM chemical potential (which corresponds to the minimal dopant formation energy) is capped by the heat of formation of $TMSe_2$. We find that the minimal formation energy of a substitutional TM dopant in $WSe_2$ is determined by the competition between the TM dopant incorporation in $WSe_2$ and the formation of the secondary phase $TMSe_2$, which, in turn, is strongly affected by the different crystal environments of TM dopants and consequently different crystal field splitting and electron filling in TM $d$ levels in $WSe_2$ and their secondary phases. Our results and insights on the TM doping efficiency in bulk $WSe_2$ should also be relevant to the understanding of TM doping in monolayer and few-layer $WSe_2$ and other TMDs.

## ACKNOWLEDGMENTS

The work at ORNL was supported by the U. S. Department of Energy, Office of Science, Basic Energy Sciences, Materials Sciences, and Engineering Division. D. Han and S. Chen were supported by the State Scholarship Fund in China and CC of ECNU. Haixuan Xu was supported by the Organized Research Unit Program (Grant No. ORU-IMHM-18) at the University of Tennessee.

[1] H. Fang, S. Chuang, T. C. Chang, K. Takei, T. Takahashi, and A. Javey, High-performance single layered $WSe_2$ $p$-FETs with chemically doped contacts, Nano Lett. **12**, 3788 (2012).

[2] H. Qiu, L. Pan, Z. Yao, J. Li, Y. Shi, and X. Wang, Electrical characterization of back-gated bi-layer $MoS_2$ field-effect transistors and the effect of ambient on their performances, Appl. Phys. Lett. **100**, 123104 (2012).

[3] T. Stephenson, Z. Li, B. Olsen, and D. Mitlin, Lithium ion battery applications of molybdenum disulfide ($MoS_2$) nanocomposites, Energy Environ. Sci. **7**, 209 (2014).

[4] E. Yang, H. Ji, and Y. Jung, Two-dimensional transition metal dichalcogenide monolayers as promising sodium ion battery anodes, J. Phys. Chem. C **119**, 26374 (2015).

[5] J. Feng, X. Sun, C. Wu, L. Peng, C. Lin, S. Hu, J. Yang, and Y. Xie, Metallic few-layered $VS_2$ ultrathin nanosheets: High two-dimensional conductivity for in-plane supercapacitors, J. Am. Chem. Soc. **133**, 17832 (2011).

[6] Y. Yang, H. Fei, G. Ruan, C. Xiang, and J. M. Tour, Edge-oriented $MoS_2$ nanoporous films as flexible electrodes for hydrogen evolution reactions and supercapacitor devices, Adv. Mater. **26**, 8163 (2014).

[7] M. Bernardi, M. Palummo, and J. C. Grossman, Extraordinary sunlight absorption and one nanometer thick photovoltaics using two-dimensional monolayer materials, Nano Lett. **13**, 3664 (2013).

[8] M.-L. Tsai, S.-H. Su, J.-K. Chang, D.-S. Tsai, C.-H. Chen, C.-I. Wu, L.-J. Li, L.-J. Chen, and J.-H. He, Monolayer $MoS_2$ heterojunction solar cells, ACS Nano **8**, 8317 (2014).

[9] X. Chia, A. Ambrosi, Z. Sofer, J. Luxa, and M. Pumera, Catalytic and charge transfer properties of transition metal dichalcogenides arising from electrochemical pretreatment, ACS Nano **9**, 5164 (2015).

[10] T. F. Jaramillo, K. P. Jørgensen, J. Bonde, J. H. Nielsen, S. Horch, and I. Chorkendorff, Identification of active edge sites for electrochemical $H_2$ evolution from $MoS_2$ nanocatalysts, Science **317**, 100 (2007).

[11] W. Choi, N. Choudhary, G. H. Han, J. Park, D. Akinwande, and Y. H. Lee, Recent development of two-dimensional transition metal dichalcogenides and their applications, Mater. Today **20**, 116 (2017).

[12] M. Chhowalla, H. S. Shin, G. Eda, L.-J. Li, K. P. Loh, and H. Zhang, The chemistry of two-dimensional layered transition metal dichalcogenide nanosheets, Nat. Chem. **5**, 263 (2013).

[13] A. K. Geim and I. V. Grigorieva, Van der Waals heterostructures, Nature **499**, 419 (2013).

[14] H. Zhu, Y. Wang, J. Xiao, M. Liu, S. Xiong, Z. J. Wong, Z. Ye, Y. Ye, X. Yin, and X. Zhang, Observation of piezoelectricity in free-standing monolayer $MoS_2$, Nat. Nanotechnol. **10**, 151 (2015).

[15] C. Chiritescu, D. G. Cahill, N. Nguyen, D. Johnson, A. Bodapati, P. Keblinski, and P. Zschack, Ultralow thermal conductivity in disordered, layered $WSe_2$ crystals, Science **315**, 351 (2007).

[16] P. Rivera, K. L. Seyler, H. Yu, J. R. Schaibley, J. Yan, D. G. Mandrus, W. Yao, and X. Xu, Valley-polarized exciton dynamics in a 2D semiconductor heterostructure, Science **351**, 688 (2016).

[17] G. Fiori, F. Bonaccorso, G. Iannaccone, T. Palacios, D. Neumaier, A. Seabaugh, S. K. Banerjee, and L. Colombo, Electronics based on two-dimensional materials, Nat. Nanotechnol. **9**, 768 (2014).

[18] M. Chhowalla, D. Jena, and H. Zhang, Two-dimensional semiconductors for transistors, Nat. Rev. Mater. **1**, 16052 (2016).

[19] P. Luo, F. Zhuge, Q. Zhang, Y. Chen, L. Lv, Y. Huang, H. Li, and T. Zhai, Doping engineering and functionalization of two-dimensional metal chalcogenides, Nanoscale Horiz. **4**, 26 (2019).

[20] H. Yuan *et al.*, Evolution of the valley position in bulk transition-metal chalcogenides and their monolayer limit, Nano Lett. **16**, 4738 (2016).

[21] L. Upadhyayula, J. Loferski, A. Wold, W. Giriat, and R. Kershaw, Semiconducting properties of single crystals of *n*-and *p*-type tungsten diselenide ($WSe_2$), J. Appl. Phys. **39**, 4736 (1968).

[22] M. Deshpande, J. Patel, N. N. Pandya, M. Parmar, and G. Solanki, Growth and transport property measurements of rhenium doped tungsten diselenide single crystal, Mater. Chem. Phys. **117**, 350 (2009).

[23] M. Agarwal, V. Rao, and V. Pathak, Growth of *n*-type and *p*-type $WSe_2$ crystals using $SeCl_4$ transporter and their characterization, J. Cryst. Growth **97**, 675 (1989).

[24] F. R. F. Fan and A. J. Bard, Photoassisted scanning tunneling microscopy and tunneling spectroscopy of *n*-type tungsten diselenide single crystals, J. Phys. Chem. **97**, 1431 (1993).

[25] S. El-Mahalawy and B. Evans, Temperature dependence of the electrical conductivity and hall coefficient in 2H-$MoS_2$, $MoSe_2$, $WSe_2$, and $MoTe_2$, Phys. Status Solidi (b) **79**, 713 (1977).

[26] W. Hicks, Semiconducting behavior of substituted tungsten diselenide and its analogues, J. Electrochem. Soc. **111**, 1058 (1964).

[27] R. Mukherjee, H. Chuang, M. Koehler, N. Combs, A. Patchen, Z. Zhou, and D. Mandrus, Substitutional Electron and Hole Doping of $WSe_2$: Synthesis, Electrical Characterization, and Observation of Band-to-Band Tunneling, Phys. Rev. Appl. **7**, 034011 (2017).

[28] Y. Fu, M. Long, A. Gao, Y. Wang, C. Pan, X. Liu, J. Zeng, K. Xu, L. Zhang, E. Liu, W. Hu, X. Wang, and F. Miao, Intrinsic *p*-type W-based transition metal dichalcogenide by substitutional Ta-doping, Appl. Phys. Lett. **111**, 043502 (2017).

[29] S. K. Pandey, H. Alsalman, J. G. Azadani, N. Izquierdo, T. Low, and S. A. Campbell, Controlled *p*-type substitutional doping in large-area monolayer $WSe_2$ crystals grown by chemical vapor deposition, Nanoscale **10**, 21374 (2018).

[30] M. Deshpande, P. Patel, M. Vashi, and M. Agarwal, Effect of intercalating indium in $WSe_2$ single crystals, J. Cryst. Growth **197**, 833 (1999).

[31] M. Deshpande, M. Parmar, N. N. Pandya, S. Chaki, and S. V. Bhatt, Studies on transport properties of copper doped tungsten diselenide single crystals, Phys. B **407**, 808 (2012).

[32] P. Zhao, D. Kiriya, A. Azcatl, C. Zhang, M. Tosun, Y. S. Liu, M. Hettick, J. S. Kang, S. McDonnell, K. C. Santosh, J. Guo, K. Cho, R. M. Wallace, and A. Javey, Air stable *p*-doping of $WSe_2$ by covalent functionalization, ACS Nano **8**, 10808 (2014).

[33] C.-H. Chen, C.-L. Wu, J. Pu, M.-H. Chiu, P. Kumar, T. Takenobu, and L.-J. Li, Hole mobility enhancement and *p*-doping in monolayer $WSe_2$ by gold decoration, 2D Mater. **1**, 034001 (2014).

[34] H. Fang, M. Tosun, G. Seol, T. C. Chang, K. Takei, J. Guo, and A. Javey, Degenerate *n*-doping of few-layer transition metal dichalcogenides by potassium, Nano Lett. **13**, 1991 (2013).

[35] R. Ovcharenko, Y. Dedkov, and E. Voloshina, Adsorption of $NO_2$ on $WSe_2$: DFT and photoelectron spectroscopy studies, J. Phys.: Condens. Matter **28**, 364003 (2016).

[36] D. H. Kang, M.-S. Kim, J. Shim, J. Jeon, H.-Y. Park, W.-S. Jung, H.-Y. Yu, C.-H. Pang, S. Lee, and J.-H. Park, High-performance transition metal dichalcogenide photodetectors enhanced by self-assembled monolayer doping, Adv. Funct. Mater. **25**, 4219 (2015).

[37] I. Lee, S. Rathi, L. Li, D. Lim, M. A. Khan, E. Kannan, and G.-H. Kim, Non-degenerate *n*-type doping by hydrazine treatment in metal work function engineered $WSe_2$ field-effect transistor, Nanotechnology **26**, 455203 (2015).

[38] D.-H. Kang, J. Shim, S. K. Jang, J. Jeon, M. H. Jeon, G. Y. Yeom, W. S. Jung, Y. H. Jang, S. Lee, and J. H. Park, Controllable nondegenerate *p*-type doping of tungsten diselenide by octadecyltrichlorosilane, ACS Nano **9**, 1099 (2015).

[39] J. Yu, C.-H. Lee, D. Bouilly, M. Han, P. Kim, M. L. Steigerwald, X. Roy, and C. Nuckolls, Patterning superatom dopants on transition metal dichalcogenides, Nano Lett. **16**, 3385 (2016).

[40] C. J. Benjamin, S. Zhang, and Z. Chen, Controlled doping of transition metal dichalcogenides by metal work function tuning in phthalocyanine compounds, Nanoscale **10**, 5148 (2018).

[41] Y. Zhao, K. Xu, F. Pan, C. Zhou, F. Zhou, and Y. Chai, Doping, contact and interface engineering of two-dimensional layered transition metal dichalcogenides transistors, Adv. Funct. Mater. **27**, 1603484 (2017).

[42] S. Liu, S. Huang, H. Li, Q. Zhang, C. Li, X. Liu, J. Meng, and Y. Tian, Tunable electronic behavior in 3d transition metal doped 2H-$WSe_2$, Phys. E **87**, 295 (2017).

[43] H. Li, S. Liu, S. Huang, Q. Zhang, C. Li, X. Liu, J. Meng, and Y. Tian, Metallic impurities induced electronic transport in $WSe_2$: First-principle calculations, Chem. Phys. Lett. **658**, 83 (2016).

[44] P. Hohenberg and W. Kohn, Inhomogeneous electron gas, Phys. Rev. **136**, B864 (1964).

[45] W. Kohn and L. J. Sham, Self-consistent equations including exchange and correlation effects, Phys. Rev. **140**, A1133 (1965).

[46] G. Kresse and J. Furthmuller, Efficient iterative schemes for ab initio total-energy calculations using a plane-wave basis set, Phys. Rev. B **54**, 11169 (1996).

[47] G. Kresse and D. Joubert, From ultrasoft pseudopotentials to the projector augmented-wave method, Phys. Rev. B **59**, 1758 (1999).

[48] J. P. Perdew, K. Burke, and M. Ernzerhof, Generalized Gradient Approximation Made Simple, Phys. Rev. Lett. **77**, 3865 (1996).

[49] J. Heyd, G. E. Scuseria, and M. Ernzerhof, Hybrid functionals based on a screened Coulomb potential, J. Chem. Phys. **118**, 8207 (2003).

[50] S. Grimme, Semiempirical GGA-type density functional constructed with a long-range dispersion correction, J. Comput. Chem. **27**, 1787 (2006).

[51] A. Alkauskas, P. Broqvist, and A. Pasquarello, Defect Energy Levels in Density Functional Calculations: Alignment and Band Gap Problem, Phys. Rev. Lett. **101**, 046405 (2008).

[52] H.-P. Komsa and A. Pasquarello, Assessing the accuracy of hybrid functionals in the determination of defect levels: Application to the As antisite in GaAs, Phys. Rev. B **84**, 075207 (2011).

[53] A. Alkauskas and A. Pasquarello, Band-edge problem in the theoretical determination of defect energy levels: The O vacancy in ZnO as a benchmark case, Phys. Rev. B **84**, 125206 (2011).

[54] A. Jain, S. P. Ong, G. Hautier, W. Chen, W. D. Richards, S. Dacek, S. Cholia, D. Gunter, D. Skinner, G. Ceder, and K. A. Persson, Commentary: The Materials Project: A materials genome approach to accelerating materials innovation, APL Mater. **1**, 011002 (2013)..

[55] J.-Y. Noh, H. Kim, and Y.-S. Kim, Stability and electronic structures of native defects in single-layer $MoS_2$, Phys. Rev. B **89**, 205417 (2014).

[56] H.-P. Komsa and A. V. Krasheninnikov, Native defects in bulk and monolayer $MoS_2$ from first principles, Phys. Rev. B **91**, 125304 (2015).

[57] H. Shi and M.-H. Du, Shallow halogen vacancies in halide optoelectronic materials, Phys. Rev. B **90**, 174103 (2014).

[58] See Supplemental Material at http://link.aps.org/supplemental/10.1103/PhysRevApplied.12.034038 for the calculated enthalpies of formation for $WSe_2$ and various dopant-related secondary phases as well as the formation energies for selected dopants.

[59] J. Wildervanck and F. Jellinek, The dichalcogenides of technetium and rhenium, J. Less Common Met. **24**, 73 (1971).

[60] B. Jariwala, D. Voiry, A. Jindal, B. A. Chalke, R. Bapat, A. Thamizhavel, M. Chhowalla, M. Deshmukh, and A. Bhattacharya, Synthesis and characterization of $ReS_2$ and $ReSe_2$ layered chalcogenide single crystals, Chem. Mater. **28**, 3352 (2016).

[61] H. Vaterlaus, R. Bichsel, F. Levy, and H. Berger, $RuS_2$ and $RuSe_2$ single crystals: A study of phonons, optical absorption and electronic properties, J. Phys. C: Solid State Phys. **18**, 6063 (1985).

[62] B. Müller and H. Lutz, Single crystal raman studies of pyrite-type $RuS_2$, $RuSe_2$, $OsS_2$, $OsSe_2$, $PtP_2$, and $PtAs_2$, Phys. Chem. Miner. **17**, 716 (1991).

[63] K. Wang, A. Wang, A. Tomic, L. Wang, A. M. M. Abeykoon, E. Dooryhee, S. J. L. Billinge, and C. Petrovic, Enhanced thermoelectric power and electronic correlations in $RuSe_2$, APL Mater. **3**, 041513 (2015).